catalysts

MDPI

Article

Synthesis of Catalytic Precursors Based on Mixed Ni-Al Oxides by Supercritical Antisolvent Co-Precipitation

Nikolay S. Nesterov, Vera P. Pakharukova, Alexey A. Philippov, Evgeny Y. Gerasimov, Sergey V. Tsybulya * and Oleg N. Martyanov

Boreskov Institute of Catalysis, Siberian Brunch of the Russian Academy of Sciences, Pr. Lavrentieva 5, 630090 Novosibirsk, Russia

* Correspondence: tsybulya@catalysis.ru

Abstract: Mixed Ni-Al oxide catalytic precursors with different elemental ratios (20, 50, and 80 wt.% Ni^0) were synthesized using green supercritical antisolvent co-precipitation (SAS). The obtained oxide precursors and metal catalysts were characterized in detail by X-ray diffraction (XRD) analysis, atomic pair distribution function (PDF) analysis, CO adsorption, and high-resolution transmission electron microscopy (HRTEM). It was found that the composition and structure of the Ni-Al precursors are related to the Ni content. The mixed $Ni_{1-x}Al_xO$ oxide with NiO-based crystal structure was formed in the Ni-enriched sample, whereas the highly dispersed $NiAl_2O_4$ spinel was observed in the Al-enriched sample. The obtained metal catalysts were tested in the process of anisole H_2-free hydrogenation. 2-PrOH was used as a hydrogen donor. The catalyst with 50 wt.% Ni^0 demonstrated the highest activity in the hydrogenation process.

Keywords: supercritical antisolvent; heterogeneous catalysts; green chemistry; nickel catalyst; mixed oxides

check for updates

Citation: Nesterov, N.S.; Pakharukova, V.P.; Philippov, A.A.; Gerasimov, E.Y.; Tsybulya, S.V.; Martyanov, O.N. Synthesis of Catalytic Precursors Based on Mixed Ni-Al Oxides by Supercritical Antisolvent Co-Precipitation. *Catalysts* **2022**, *12*, 1597. https://doi.org/10.3390/catal12121597

Academic Editors: Alexander Kokorin and Detlef W. Bahnemann

Received: 28 October 2022
Accepted: 3 December 2022
Published: 6 December 2022

Publisher's Note: MDPI stays neutral with regard to jurisdictional claims in published maps and institutional affiliations.

1. Introduction

Mixed Ni-Al oxide systems are of interest as precursors of metallic Ni-containing catalysts [1–3]. The strong interaction between nickel cations and aluminum oxide often leads to the formation of spinel phases, which complicates the process of reduction and formation of the metallic nickel phase [4,5]. However, this interaction hinders the sintering processes, which makes it possible to obtain more highly dispersed systems in comparison with other oxide supports [6,7]. It has also been shown in a number of studies that the strong interaction of nickel metal particles with aluminum oxide suppresses coke formation in the dry reforming of methane and thereby increases the stability of the catalyst [8–10].

The most common methods of Ni-Al_2O_3 catalyst synthesis are impregnation [11], deposition-precipitation [12], and the sol-gel method [13]. The disadvantages of these synthesis methods are the use of toxic nitrates and the formation of wastewater, which require additional processing. One of the rapidly growing green approaches to the catalyst synthesis is the transition to supercritical fluid (SCF) technology [14,15]. CO_2 is fire safe, cheap, non-toxic, and has low critical parameters (T_c = 30.6 °C, P_c = 73.8 bar), which makes it attractive as a green solvent for the synthesis of various functional materials [16,17]. One of the promising SCF approaches to the synthesis of heterogeneous catalysts is Supercritical AntiSolvent (SAS) precipitation, which avoids the use of toxic nitrates and the production of aqueous waste [18]. The high value of supersaturation, which is obtained by SAS precipitation, can lead to the formation of phases that are difficult to synthesize using other approaches [19]. For example, SAS precipitation was used to synthesize mixed Cu-Zn hydroxocarbonate with georgeite structure, the obtained catalysts exhibited high activity in the methanol production [20] and in the water gas shift reaction [21]. In addition, SAS was used to synthesize highly active systems for photooxidation based on ZnO [22] and TiO_2 [23,24].

The promising results in catalyst preparation via SAS precipitation has been demonstrating in our recent studies. We have proposed an original approach to the synthesis of metal catalysts, which is based on SAS co-precipitation of stable oxide sols [25] and the addition of water cosolvent, as a tool to enhance metal mixing and avoid phase separation [26]. The oxide sols formed a matrix to stabilize Ni catalysts [27] and Au nanomaterials [28,29]. Series of Ni-Cu catalysts for anisole hydrodeoxygenation were synthesized by SAS co-precipitation [30,31].

In this work, we synthesized highly dispersed mixed Ni-Al oxide precursors using the SAS co-precipitation method to obtain metallic Ni catalysts with different metal loadings. The Ni-Al oxide precursors and metal Ni-Al catalysts were thoroughly characterized; the features of the active phase formation were investigated. This technique was shown to allow obtaining highly dispersed Ni catalysts with a high content of the active metal phase. The catalysts were tested in the process of H_2-free hydrogenation of anisole, a model compound of pyrolysis liquid [32]. H_2-free hydrogenation is based on the idea that simple organic molecules such as formic acid [33], cycloalkenes [34] or alcohols [35] can be used instead of H_2. It provides some important advantages due to their comparatively low flammability, low corrosive activity, and liquid aggregate state. We chose 2-PrOH as a hydrogen donor because it demonstrates activity in H_2-free hydrogenation using Ni-containing catalysts [36–39]. It is important to notice that lower aliphatic alcohols, which can also be obtained from biomass [40] as well as phenolic compounds, are often used as hydrogen donors for H_2-free hydrogenation [41,42].

2. Results and Discussion

2.1. Catalyst Characterization

2.1.1. Ni-Al Oxide Precursors

Figure 1 shows powder XRD patterns of Ni-Al oxide precursors. All the XRD patterns exhibit reflections corresponding to NiO crystalline phase (PDF NO. 00-047-1049) with NaCl structure type (space group $Fm\bar{3}m$). The measured crystal lattice parameters are lower than the value characteristic of NiO phase a = 0.4176 nm (Table 1). The difference is most pronounced for Ni50_Alum and Ni20_Alum samples with a high Al content. This indicates the formation of $Ni_{1-x}Al_xO$ substitutional solid solutions on the base of the NiO structure. Thus, the radius of Ni^{2+} ions in octahedral coordination is larger than that of Al^{3+} ions (0.69 vs. 0.53 Å). Observed change in intensities of 111 and 200 reflections (I_{111} and I_{200}) favors the suggestion about formation of solid solution. The I_{111}/I_{200} ratio is lower than that of pure NiO phase. This is illustrated by comparison of the experimental XRD patterns with XRD profiles calculated by the Rietveld refinement of NiO structure model (Figure 1). It is possible that cation vacancies are formed in the $Ni_{1-x}Al_xO$ oxide to maintain charge balance.

The average size of $Ni_{1-x}Al_xO$ crystallites in of Ni80_Alum sample is 4 nm; this sample is the most well-crystallized among all samples.

Table 1. Structural characteristics of detected $Ni_{1-x}Al_xO$ phases (s.g. $Fm\bar{3}m$) in the Ni-Al oxide precursors according to XRD analysis.

Sample	Lattice Parameter (nm)	d_{XRD} (nm)
Ni80_Alum	0.4164(1)	4.0
Ni50_Alum	0.4157(1)	2.5
Ni20_Alum	0.4147(2)	~2.5–3

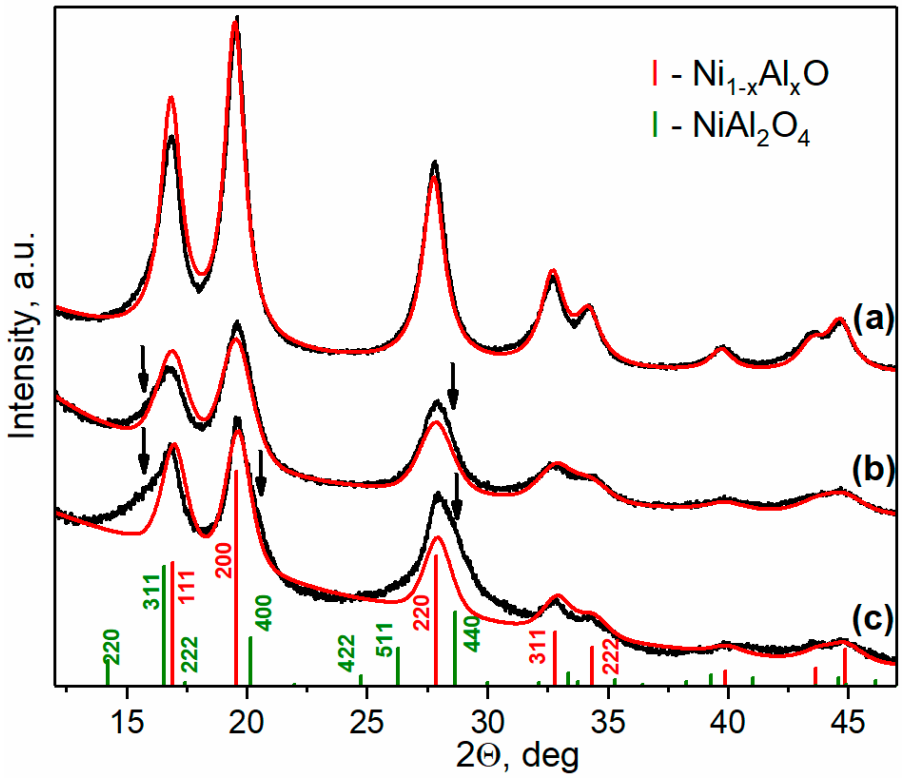

Figure 1. Experimental XRD patterns for Ni-Al oxide precursors (black lines) in comparison with XRD profiles calculated at the Rietveld refinement of NiO structure model (red lines): Ni80 _Alum—(**a**); Ni50 _Alum—(**b**); Ni20 _Alum—(**c**).

To clarify structural features of Ni-Al oxide precursors, the PDF analysis was used, as it is highly efficient for the atomic-scale study of poorly crystallized and fine materials. The positions of peaks in the PDF curve reflect interatomic distances; the peak amplitudes are related to coordination numbers. The obtained PDF for Ni20_Alum sample exhibits coordination peaks, which are characteristic of NiO oxide structure. However, the NiO structure model cannot fully describe the experimental PDF, as can be seen from fitting results presented in Figure 2a. The differences are manifested in the excess of the atomic density in the experimental PDF at distances r = 1.9, 3.2, 4.4, 6.0 Å. These distances are close to interatomic distances in the spinel structure. The model of a mixture of NiO oxide (s.g. $Fm\bar{3}m$) and $NiAl_2O_4$ spinel (s.g. $Fd\bar{3}m$) was exanimated. This "two-phase" model reproduces the experimental PDF significantly better (Figure 2b). The refined lattice parameter of the NiO phase (a = 0.4149 nm) is reduced due to the formation of $Ni_{1-x}Al_xO$ solid solution, as mentioned above. The refined average size of $Ni_{1-x}Al_xO$ crystallites is 3 nm. The refined lattice parameter of the spinel phase (a = 0.8051 nm) is close to that of $NiAl_2O_4$ crystalline phase (PDF# 00-010-0339, a = 0.8048 Å). The spinel phase is poorly crystalized; the determined average size of the atomic ordering is only 1.5 nm. Thus, PDF analysis of the local atomic structure confirmed the coexistence of two Ni-Al mixed oxides with different structures in Ni20_Alum sample. Obviously, Ni-enriched $Ni_{1-x}Al_xO$ oxide has a NiO-based structure, while the Al-enriched Ni-Al mixed oxide has a spinel-type structure. Accurate determination of cation composition in both mixed oxides is complicated.

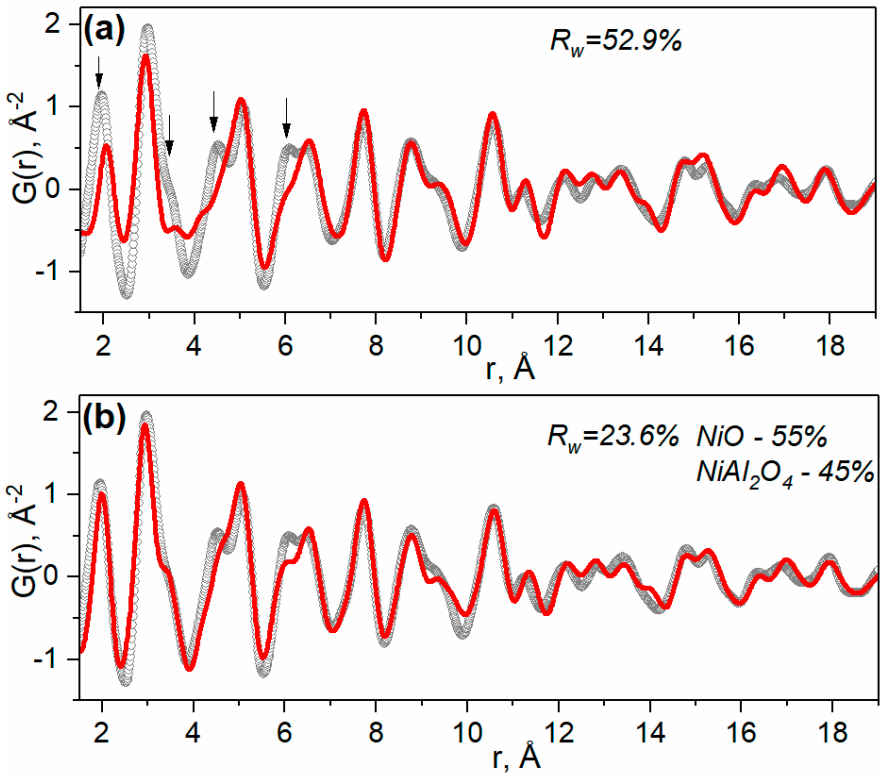

Figure 2. Observed PDF for Ni20_Alum sample (gray circles) in comparison with model PDFs (red lines). The model PDFs are calculated for NiO nanoparticles (**a**) and a mixture of NiO and $NiAl_2O_4$ nanoparticles (**b**). The corresponding disagreement factors R_w are shown.

In the case of Ni50_Alum sample, the "two-phase" model also improves fitting results, but to a lesser extent (R_w = 22.1% versus R_w = 24.8% for "single-phase" NiO model). The fitting results are presented in Figure 3a. The refined average sizes of NiO and $NiAl_2O_4$ nanoparticles are 3 and 1.5 nm, respectively. The refined content of the $NiAl_2O_4$ phase was significantly smaller (15%). Thus, the content of the spinel phase decreases with the decrease in Al content in the samples. No spinel phase was detected by PDF analysis in Ni-enriched Ni80_Alum sample. The obtained PDF for Ni80_Alum sample is fully described by the model of NiO nanoparticles of 4 nm in size.

Figure 4 shows TEM images of oxide Ni20_Alum and Ni50_Alum precursors. These samples are spherical agglomerates with sizes from 50 to 300 nm, which consist of smaller particles. In the Ni20_Alum sample, a large amount of amorphous phase is observed in the composition of agglomerates, but well-crystallized particles are also detected (Figure 4a1). In the Ni50_Alum sample, the fraction of well-crystallized particles is significantly higher than in the Ni20_Alum sample. These data correlate well with the PDF analysis data revealing a significantly higher content of poorly crystalized spinel phase in the Ni20_Alum sample compared to Ni50_Alum. The observed crystallized particles in the samples were found to have NiO-based or $NiAl_2O_4$ spinel structure. Detected interplanar distances for the Ni20_Alum sample of 1.55, 2.01 and 2.40 Å may correspond to the planes d_{511}, d_{400}, and d_{311} of the $NiAl_2O_4$ spinel phase, as well as interplanar distances of 2.01 and 2.40 Å may correspond to the planes d_{200} and d_{111} of NiO phase. The interplanar distances for the Ni50_Alum sample of 2.06 and 2.41 Å may correspond to the planes d_{200} and d_{111} of NiO phase.

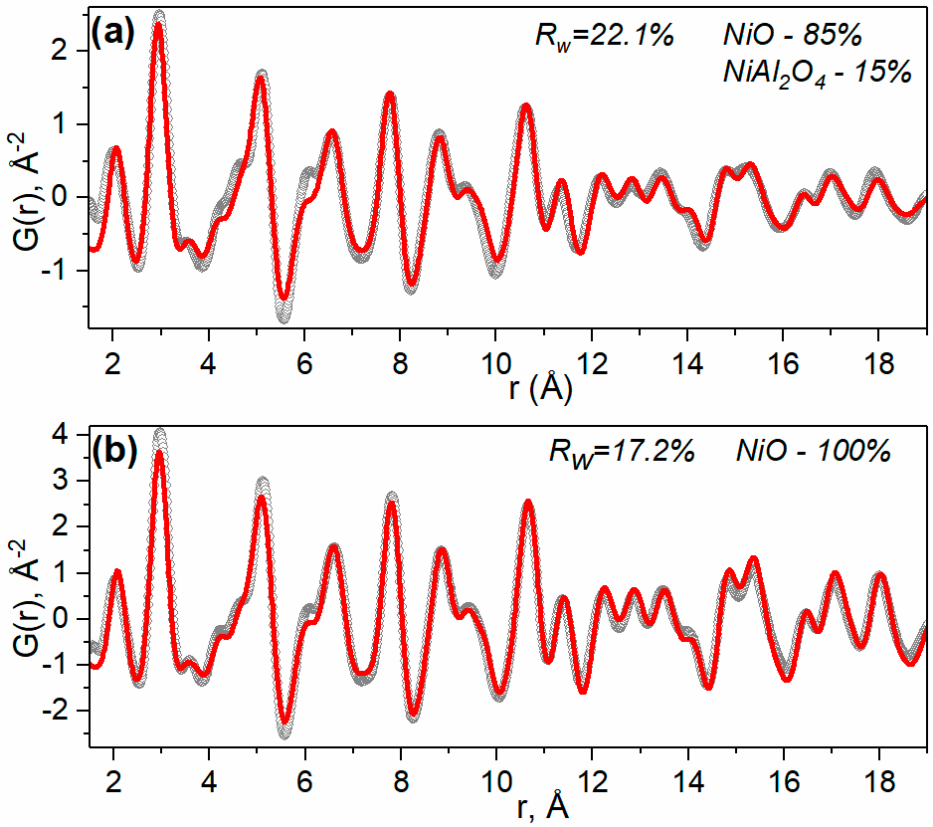

Figure 3. PDF fitting results for Ni50_Alum sample by model of the mixture of NiO and $NiAl_2O_4$ nanoparticles (**a**) and for Ni80_Alum sample by the model of NiO nanoparticles (**b**). Gray circles and red lines indicate observed and model PDFs, respectively.

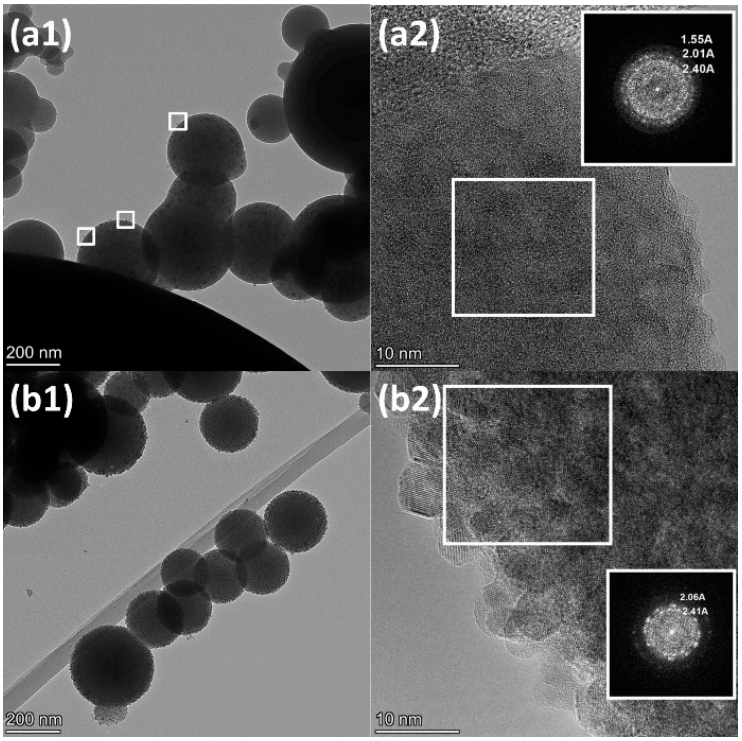

Figure 4. TEM, HRTEM images and FFT patterns of Ni-Al oxide precursors: Ni20_Alum—(**a1**,**a2**); Ni50_Alum—(**b1**,**b2**).

2.1.2. Reduced Ni-Al Catalysts

According to the H_2-TPR data (Figure 5), the reduction in the Ni80_Alum sample proceeds at a lower temperature (the maximum of the H_2-TPR peak is 480 °C) than the reduction in the Ni50_Alum and Ni20_Alum samples (the maxima of the H_2-TPR peaks are 555 °C). Decrease in nickel content from 80 to 50 wt.% leads to difficulties in the nickel reduction process. However, a further decrease in the nickel content in the samples practically does not affect the character of the H_2-TPR profiles; for the Ni50_Alum and Ni20_Alum samples, they are almost identical.

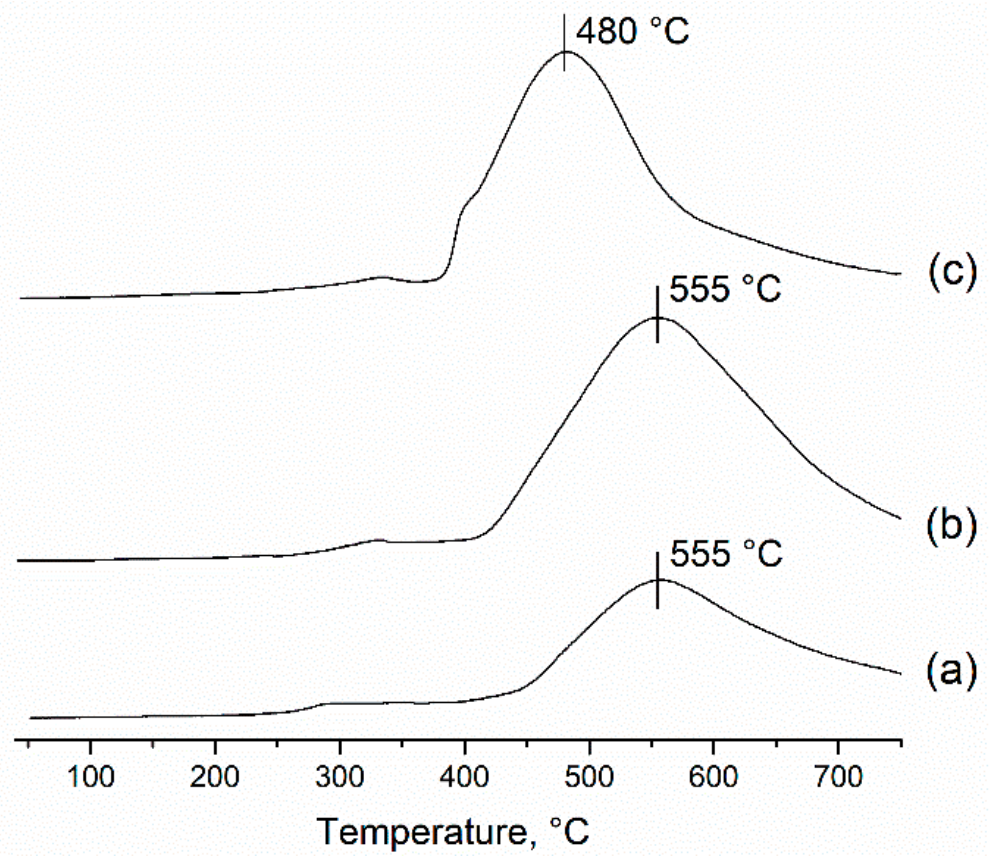

Figure 5. H_2-TPR profiles of Ni-Al oxide precursors: Ni20_Alum—(**a**); Ni50_Alum—(**b**); Ni80_Alum—(**c**).

Table 2 shows the nickel content data determined by inductively coupled plasma–atomic emission spectroscopy (ICP-AES). In all samples, there is an excess nickel content relative to the theoretical content. It is likely that the process of aluminum tri-sec-butoxide hydrolysis may not proceed completely, or the aluminum tri-sec-butoxide itself may partially hydrolyze, which leads to a decrease in the concentration of aluminum oxide in the sol.

Table 2. Structural characteristics of crystalline phases in Ni-Al catalysts according to XRD analysis.

Sample	Ni^0			Al_2O_3	
	Lattice Parameter (nm)	d_{XRD} (nm)	Ni Content, wt.%	Lattice Parameter (nm)	d_{XRD} (nm)
Ni80_Alum	0.3524(1)	15.5	85.6	-	-
Ni50_Alum	0.3523(1)	6.5	57.8	-	<2.5
Ni20_Alum	0.3526(1)	3.5	26.8	0.7951(2)	~2.5

The XRD patterns for reduced Ni-Al samples exhibit peaks attributed to metallic Ni^0 phase (Figure 6). The determined lattice parameters (Table 2) coincide with the value characteristic of Ni^0 phase (PDF NO. 04-0850, a = 0.3524 nm). This implies that the formed under reduction metallic Ni^0 phase is not doped with Al. The absence of reflections from Ni-enriched $Ni_{1-x}Al_xO$ oxide indicates its decomposition caused by the Ni loss. The reflections from the oxide with a spinel structure are observed in XRD patterns for Ni20_Alum and Ni50_Alum samples. The determined lattice constant a = 0.7951 nm of the spinel phase in Ni20_Alum sample is close to that for Al_2O_3 oxide (0.7830–0.7940 nm). This implies that Ni atoms leave the spinel structure of Al-enriched Ni-Al mixed oxide under reducing conditions with remaining pure or slightly Ni doped Al_2O_3 oxide. Therefore, one can conclude that nickel leaves the structure of both Ni-enriched $Ni_{1-x}Al_xO$ oxide and Al-enriched Ni-Al oxide with spinel structure with formation of metallic Ni^0 nanoparticles.

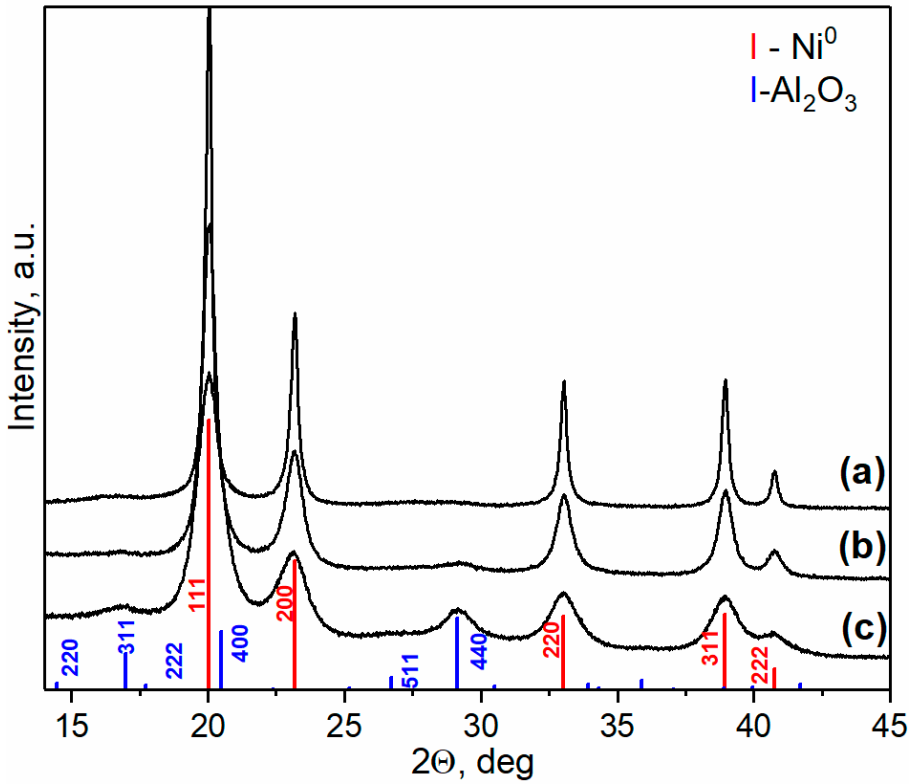

Figure 6. Experimental XRD patterns for reduced Ni-Al catalysts: Ni80_Alum (**a**); Ni50_Alum (**b**); Ni20_Alum (**c**).

A considerable difference in average size of Ni^0 crystallites in the Ni-Al catalysts was detected (Table 2). It is known that NiO oxide is more reducible than $NiAl_2O_4$ spinel and Ni^0 particles formed from NiO are sintered more than those from $NiAl_2O_4$ [43]. For this reason, the Ni20_Alum catalyst contains highly dispersed Ni^0 crystallites produced from hardly reducible $NiAl_2O_4$ spinel phase, while Ni80_Alum catalyst contains significantly larger Ni^0 crystallites formed from prevailing $Ni_{1-x}Al_xO$ oxide (Table 2).

2.2. Transfer Hydrogenation of Anisole

Chemical transformations of anisole are of interest because this compound is used as a model O-containing object of bio-oil components [44]. The low activity of anisole in hydrogenation processes [38] also makes it a good model compound for the processing of bio-oil.

Figure 7 shows the scheme of anisole transformations under hydrogen transfer conditions using the obtained catalysts. According to experimental data, the conversion of

anisole and the formation of products proceed along four parallel paths. The final products of transformation under these conditions are cyclohexane (CHA), methoxycyclohexane (MCA), cyclohexanol (CHL), and isopropyl cyclohexyl ether (ICE) (Figure 8). Benzene (BEN) is formed by the bond cleavage between the O-CH_3 group and the aromatic group, and BEN is an intermediate product formed by the first transformation pathway. From the experimental and calculated data presented in Figure 8, it can be concluded that the use of Ni50_Alum and Ni80_Alum catalysts leads to an almost complete conversion of anisole. It should also be noted that the content of the main MCA product is 75% and 64% at using the Ni80_Alum and Ni50_Alum catalyst, respectively. The deoxygenation process proceeds best over the Ni50_Alum catalyst: the content of the main deoxygenation product, CHA, is the highest among all the catalysts (26%). It is important to notice that mass balance calculated using the internal standard was in the range of 98–106% for all the experiments.

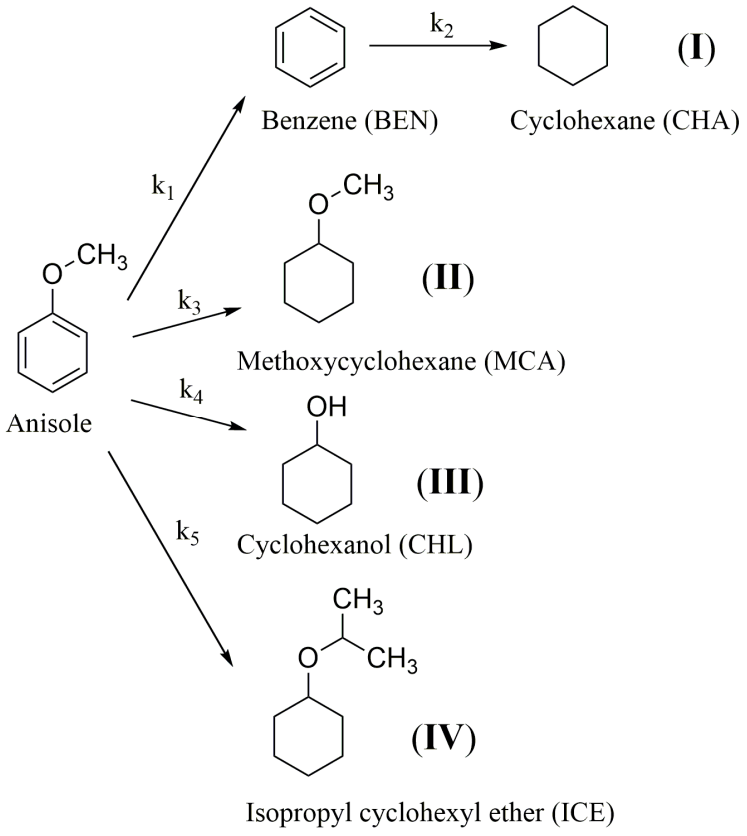

Figure 7. Scheme of transformations of anisole and intermediates over Ni-based catalysts (k_i are the quasi-first order rate constants). The experiments were carried out at T = 250 °C, P = 7.1–7.8 MPa.

Table 3 shows the calculated rate constants of chemical transformations. The Ni50_Alum catalyst has the highest total anisole conversion constant ($k_1 + k_3 + k_4 + k_5 = 5.72 \times 10^{-4}$ s^{-1}). It should be noted that the rate constant characterizing the second path of the anisole-to-MCA transformation is the largest for the Ni80_Alum catalyst. For all the catalysts, the rate constant k_2 has the highest value among all other constants. This means that the hydrogenation of BEN into CHA over these catalysts is the fastest process.

In addition, Table 3 shows the values of the rate constants normalized by the surface area of the metal Ni^0. The close values of the specific constants k_{2S} (or k_{5S}) for all catalysts probably indicate that the limiting stage of the CHA (or ICE) formation occurs on the surface of metallic nickel and, accordingly, the rate constants of these transformations directly depend on the value of the specific surface of metallic Ni^0. The values of the specific constants k_{1S} and k_{4S} have strong differences for the synthesized catalysts. It seems that the rate determining processes for these transformations do not occur on metal centers. An interesting pattern is observed for the specific constant k_{3S}. Its value increases with the increasing

loading of metallic Ni^0. For the second path of transformation, an increase in the size of Ni^0 crystallites probably contributes to the process of anisole-to-MCA hydrogenation.

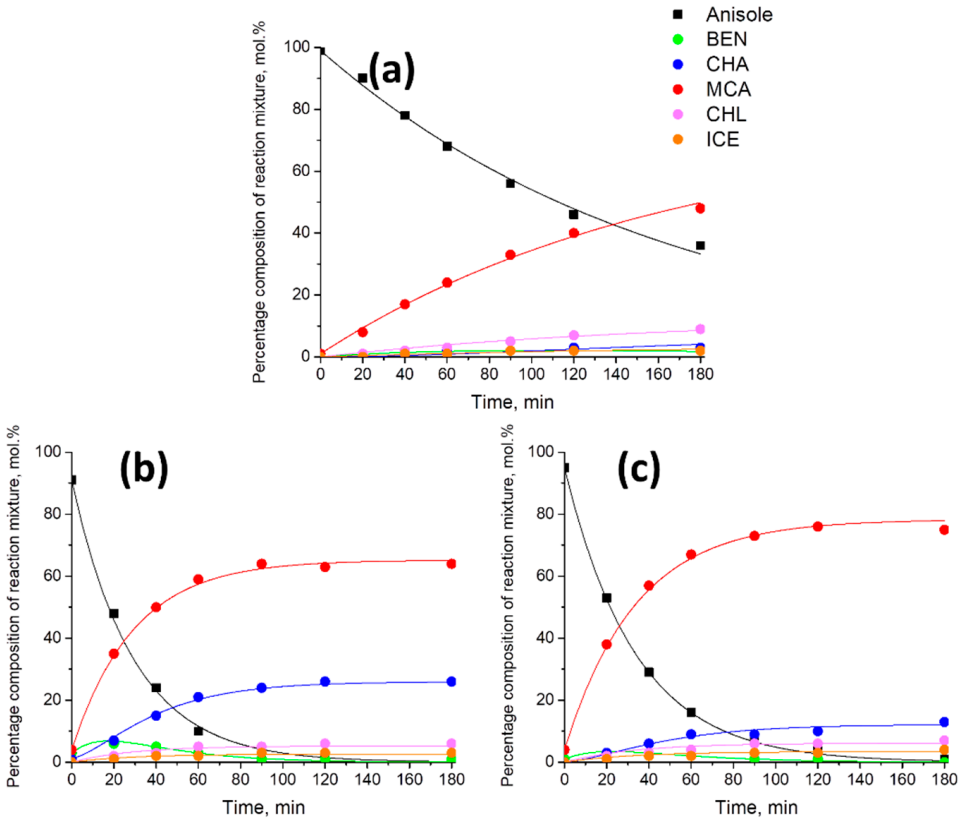

Figure 8. Composition of reaction mixtures as a function of time. The experiments were carried out at T = 250 °C, P = 7.1–7.8 MPa. The catalysts used: Ni20_Alum (**a**); Ni50_Alum (**b**); Ni80_Alum (**c**). The points are experimental data and the lines are data calculated from the quasi-first order kinetic model.

Table 3. Rate constants and specific rate constants of the product formation in the experiments at 250 °C. Specific rate constants normalized to the surface of metallic Ni $k_{iS} = k_i / A_{CO}$.

Rate Constants					
Sample	$k_1 \times 10^4$, s^{-1}	$k_2 \times 10^4$, s^{-1}	$k_3 \times 10^4$, s^{-1}	$k_4 \times 10^4$, s^{-1}	$k_5 \times 10^4$, s^{-1}
Ni20_Alum	0.09 ± 0.01	2.23 ± 0.58	0.75 ± 0.01	0.13 ± 0.01	0.04 ± 0.01
Ni50_Alum	1.38 ± 0.03	10.15 ± 0.75	3.85 ± 0.05	0.33 ± 0.02	0.16 ± 0.02
Ni80_Alum	0.58 ± 0.02	8.18 ± 1.19	3.87 ± 0.05	0.32 ± 0.02	0.18 ± 0.02
Specific rate constants					
Sample	$k_{1S} \times 10^4$, $s^{-1} \times m^{-2}$	$k_{2S} \times 1\,0^4$, $s^{-1} \times m^{-2}$	$k_{3S} \times 10^4$, $s^{-1} \times m^{-2}$	$k_{4S} \times 10^4$, $s^{-1} \times m^{-2}$	$k_{5S} \times 10^4$, $s^{-1} \times m^{-2}$
Ni20_Alum	0.16 ± 0.02	4.05 ± 1.05	1.36 ± 0.02	0.24 ± 0.02	0.07 ± 0.02
Ni50_Alum	0.62 ± 0.01	4.58 ± 0.34	1.74 ± 0.02	0.15 ± 0.01	0.07 ± 0.01
Ni80_Alum	0.33 ± 0.01	4.71 ± 0.69	2.23 ± 0.03	0.18 ± 0.01	0.10 ± 0.01

Low reactivity of anisole in heterogeneous catalytic transfer hydrodeoxygenation significantly limits a number of the relevant works. However, transformations of anisole under transfer hydrogenation conditions were considered in some studies [6,45]. For example, our recent work demonstrated the effect of catalyst supports on catalytic activity and selectivity [6]. It has been shown that Ni-SiO_2 has the highest TOF, which achieves 0.49 s^{-1} vs. 0.42 s^{-1} for Ni-Al_2O_3. However, alumina supported catalyst demonstrated

superior selectivity of hydrodeoxygenation resulting in high cyclohexane yield. The choice of Ni-Al_2O_3 as catalyst in this study was based on this fact. Other study looked at some mechanistic aspects of anisole and other biomass-like compounds transfer hydrogenation over oxide-supported Ru-based catalysts [45]. DFT calculations and experimental results demonstrated the positive effect of acidic centers on cyclohexanol yield, whilst the rate of cyclohexane formation remained low. Thus, the results obtained in the current study significantly expands the understanding the relationship between catalyst structure and its activity.

Conventional reduction is paid much more attention compared to transfer hydrogenation. For example, it has been demonstrated that Ni-USY shows the highest selectivity to cyclohexane compared to Ru-USY and Pd-USY at 200 °C under 52 atm of H_2, however, catalytic activity of the Ni-based catalyst remains comparatively low [44]. In addition, in transfer hydrogenation, a support plays an important role in conventional processes. The comparison of Ni/TiO_2 and Ni/TiO_2-ZrO_2 in anisole hydrogenation at 300 °C demonstrated that the ZrO_2 changes the structure of the support that leads to smaller Ni crystallites and higher concentration of surface acids, promoting the conversion of anisole [46]. This corroborates with the results of other studies [47,48] and the current work. Further, regarding the catalyst structure, the mean size of nickel crystallites can be controlled by the metal loading [49,50].

3. Materials and Methods

3.1. Reagents

Anisole (99%, Sigma-Aldrich, Darmstadt, Germany), dodecane (≥99%, Sigma-Aldrich, Shandong Lanhai Industry Co., Ltd., Jinan, China), 2-PrOH (≥99.5%, EKOS-1, Moscow region, Russia), nickel acetate ($Ni(OAc)_2 \cdot 4H_2O$, 99% extra, Acros Organics, Geel, Belgium), methanol (HPLC Gradient Grade, J.T. Barker, Deventer, The Netherlands), CO_2 (99.8%, Promgazservis, Novosibirsk, Russia), aluminium tri-sec-butoxide (97%, Acros Organic, Geel, Belgium).

3.2. Catalysts Synthesis

The synthesis of Ni-Al oxide samples was performed by supercritical antisolvent co-precipitation using a specially designed SAS-50 set-up (Waters, Milford, MA, USA). A methanol solution containing nickel acetate and alumina sol was injected into a stream of supercritical carbon dioxide. The solvent power of the carbon dioxide-methanol mixture reduced, and precipitation occurred. After that, the pure CO_2 was passed through the obtained powder for 20 min to remove residual solvent. A detailed description of the synthesis technique is given in the work [27].

Experimental parameters: CO_2 flow 80 g/min, solution flow 2 mL/min, temperature 40 °C, nozzle 0.004" (0.10 mm), pressure 150 bar. We obtained three species designated as Ni20_Alum, Ni50_Alum, and Ni80_Alum, where the number denotes the wt.% of metallic nickel in the reduced sample. We synthesized three solutions containing nickel acetate and alumina sol.

Synthesis of Ni20_Alum solution: under constant stirring, 2.69 mL of acetylacetone was added to 12.9 mL of isopropanol, and then 3.36 mL of Aluminum-tri-sec-butoxide was added to this solution; after addition of Aluminum-tri-sec-butoxide, a white precipitate occurred. Next, 29.2 mL of methanol was added to the resulting suspension. After 15 min of stirring, the precipitate dissolved, and 1.88 mL of water was added into the resulting solution. The resulting solution was left with stirring for 24 h. The total volume of sol was 50 mL. 0.7066 g of nickel acetate was dissolved in the resulting sol.

Synthesis of Ni50_Alum solution: under constant stirring, 1.68 mL of acetylacetone was added to 15.8 mL of isopropanol, and then 2.10 mL of Aluminum-tri-sec-butoxide was added to this solution; after addition of Aluminum-tri-sec-butoxide, a white precipitate occurred. 29.2 mL of methanol was added to the resulting suspension. After 15 min of stirring, the precipitate dissolved, and 1.18 mL of water was added into the resulting

solution. The resulting solution was left with stirring for 24 h. The total volume of sol was 50 mL. 1.7670 g of nickel acetate was dissolved in the resulting sol.

Synthesis of Ni80_Alum solution: under constant stirring, 0.67 mL of acetylacetone was added to 15.3 mL of isopropanol, and then 0.84 mL of Aluminum-tri-sec-butoxide was added to this solution; after addition of Aluminum-tri-sec-butoxide, a white precipitate occurred. Then, 32.7 mL of methanol was added to the resulting suspension. After 15 min of stirring, the precipitate dissolved, and 0.47 mL of water was added into the resulting solution. The resulting solution was left with stirring for 24 h. The total volume of sol was 50 mL. 2.8262 g of nickel acetate was dissolved in the resulting sol.

The samples after SAS co-precipitation were calcined at 300 °C for 3 h with ramp rate 3 °C/min in a static air to give the oxide phase. The reduction of samples was performed in H_2 atmosphere at 650 °C for 45 min with ramp rate 3 °C/min, the flow rate of H_2 was 30 mL/min.

3.3. CO Pulse Chemisorption and H_2-Temperature Programming Reduction Measurements

CO pulse chemisorption measurements were carried out using a Chemosorb analyzer (Modern Laboratory Equipment, Novosibirsk, Russia). First, 50 mg of each catalyst was placed inside a U-shape quartz reactor and treated in an H_2 flow (100 mL/min) upon heating up to 650 °C, ramp rate 10 °C/min. The reactor was kept at the final temperature for 20 min and then purged by inert gas (Ar) followed by cooling down to room temperature. After that, pulses of CO were fed to the reactor (100 μL) until the amount of CO in the outlet stopped changing according to the thermal conductivity detector. Thereafter, the amount of chemisorbed CO was estimated.

H_2-temperature programming reduction (H_2-TPR) measurements were also carried out using a Chemosorb analyzer; 50 mg of each catalyst was placed inside a U-shape quartz reactor and treated in an flow of 10 vol.% H_2 in Argon (100 mL/min) upon heating up to 750 °C, ramp rate 10 °C/min.

3.4. ICP-AES

Inductively coupled plasma–atomic emission spectroscopy (Optima 4300-DV, PerkinElmer Inc., Wellesley, Waltham, MA, USA) was used to determine the elemental composition of the catalysts.

3.5. XRD Characterization

XRD experiments for conventional phase analysis and PDF study were carried out using MoKα radiation (λ = 0.7093 Å) on a STOE STADI MP diffractometer (STOE, Darmstadt, Germany) equipped with a one-dimensional silicon strip MYTHEN2 1K detector (Dectris AG, Baden, Switzerland). The measurements were carried out in transmission geometry in a rotating holder. Prior to the measurement, the instrument was calibrated against a NIST SRM 660c standard (LaB_6). The measurements were carried out by scanning in the range of angles 1.5–127° with a step of 0.015°. A background contribution was measured using an empty polymer foil. A maximum scattering vector value (Q_{max}) of 15.8 $Å^{-1}$ was achieved.

XRD phase analysis was performed using the ICDD PDF-2 database. The average sizes of the crystallites (d_{XRD}) were estimated by Scherrer equation. The reflections 200 and 111, 220, 220 were analyzed for NiO-based oxide phase and metal Ni^0 phase, respectively.

Analysis of atomic pair distribution functions, G(r), was performed to study local atomic structure of samples and detect highly dispersed XRD undetectable species [51]. PDF curves were calculated with use of PDFgetX2 [52]. The obtained PDFs were analyzed by fitting to them model PDFs calculated for assumed structures. PDFgui program [53] was used for the calculation of model PDFs and their fitting to the experimental PDFs. To account for the effect of finite particle sizes, the model PDF was truncated by the shape factor given for spherical particles. The discrepancy factor (R_{wp}) was used as criterion of agreement at the simulation of the PDF profiles.

3.6. HRTEM Characterization

The morphology and microstructure of the samples were studied via high resolution transmission electron microscopy (HRTEM). The images were obtained using a Themis Z electron microscope (Thermo Fisher Scientific, Eindhoven, The Netherlands) equipped with a Ceta 16 CCD sensor and a corrector of spherical aberrations, which provided a maximum lattice resolution of 0.07 nm at an accelerating voltage of 200 kV. The samples for the HRTEM study were deposited on a holey carbon film mounted on an aluminum grid by the ultrasonic dispersal of the catalyst suspension in ethanol. The calculation of interplanar distances was carried out using fast Fourier transform (FFT) patterns using Velox software (Thermo Fisher Scientific, Waltham, MA, USA) and Digital Micrograph (Gatan, Pleasanton, CA, USA).

3.7. Batch Experiments

Before the experiment, the sample of the oxidized catalyst (0.12 g) was reduced in H_2 flow (30 L/h) for 45 min. The process was carried out in the quartz tube at 650 °C. Then, the catalysts were pulled out of the furnace and cooled down to the room temperature. After that, the samples in the tube were purged with Ar and carefully replaced to the glass filled with 30 mL of 2-PrOH.

The batch reactor (AISI 316L, 285 mL) previously purged with Ar was charged by the suspension of the catalyst and 30 mL of 2-PrOH. Then, the solution including 3.2 g of anisole (29.6 mmol), 0.25–0.26 g of dodecane (internal standard), and 80 mL of 2-PrOH was added. After that, the reactor was purged with argon under stirring (mechanical agitator MagneDrive®). The reactor was closed and heated up to 250 °C for 35 min. The reaction was carried out at a constant temperature with permanent stirring at 800 rpm. Self-pressure of the reaction mixture achieved 7.1–7.8 MPa at 250 °C and 0.7–1.0 MPa at 150 °C. During the experiment, the probes of the reaction mixture were collected to the sampler. To calculate conversion the following equation was used:

$$Conversion = \frac{|Anisole|_{in} - |Anisole|_{fin}}{|Anisole|_{fin}} \times 100\% \quad (1)$$

3.8. Product Analysis

The liquid samples were analyzed using GCMS–QP2010 SE chromato-mass spectrometer (Shimadzu, Kyoto, Japan) equipped with the autosampler. The GsBP-INOWAX capillary chromatographic column (crosslinked polyethylene glycol) was used (length 30 m, internal diameter 0.32 mm, stationary phase thickness 0.25 μm). The temperature mode of column conditioning was: 55 °C for 3 min, programmed heating up to 200 °C at a rate of 15 °C per minute and then up to 270 °C at the rate of 25 °C per minute. The evaporator temperature was 270 °C, split 1:30, helium was used as a carrier gas. A constant flow rate of the carrier gas was 1.8 mL min^{-1}. The products were identified using the peak retention time and the mass spectrum of the substance, which were compared with the data from the NIST and Wiley7 electronic mass spectral libraries, or in some cases with corresponding data of pure compounds. Conversion of anisole and yield of products were evaluated using dodecane as an internal standard.

3.9. Calculations of Kinetic Data

The experimental dependence of anisole conversion was described by quasi-first order kinetics with respect to the anisole and intermediate products. The calculations were performed using the following simplified model: $dC_i/dt = k_i C_i$. Here, k_i first-order rate constant, C_i molar fraction of anisole, and other products.

The reaction rate constants were determined by the least-squares method using the obtained analytical solution. The following function was minimized:

$$F(\vec{k}) = \sum_{i,j} (c_{ij}^{exp} - c_i^{calc}(t_j, \vec{k}))^2 \quad (2)$$

where $\vec{k}$ is a vector of reaction rate constants, $\vec{k} = (k_1, k_2, k_3, k_4, k_5)$; j is the serial number of an experimental point, t_j is the time of the j-th point, c_{ij}^{exp} is the experimental molar fraction of the i-th component at time t_j, $c_i^{calc}(t_j, \vec{k})$ is the calculated molar fraction of the i-th component at time t_j. The values of $c_i^{calc}(t_j, \vec{k})$ concentrations were calculated using the Runge-Kutta method.

4. Conclusions

In this work, a series of catalytic precursors based on mixed Ni-Al oxides was synthesized using the original «green» supercritical antisolvent (SAS) co-precipitation method. It was found that mutual doping between nickel and aluminum species in the synthesized systems leads to the formation of mixed oxides with different structure and composition: $Ni_{1-x}Al_xO$ solid solution with NiO-based structure and $NiAl_2O_4$ spinel phase. The change in Ni loading altered the ratio between $Ni_{1-x}Al_xO$ and $NiAl_2O_4$ phases. Thus, the $Ni_{1-x}Al_xO$ mixed oxide was formed in Ni-enriched sample, whereas a large amount of $NiAl_2O_4$ spinel phase was detected in the Al-enriched sample.

It was shown that under reduction, nickel leaves the structure of both $Ni_{1-x}Al_xO$ oxide and $NiAl_2O_4$ spinel phase with the formation of metallic Ni^0 nanoparticles. Larger Ni^0 nanoparticles are formed from $Ni_{1-x}Al_xO$ oxide, while more dispersed particles are formed from the spinel phase.

The reduced catalysts were investigated in the process of H_2-free hydrogenation of anisole, a model compound of bio-oil. The results imply that the catalytic activity and selectivity can be tuned by the compositions of the Ni-Al oxide precursors. The sample with 50 wt.% Ni^0 demonstrated the highest activity in anisole hydrogenation, as well as the highest activity in the process of anisole deoxygenation.

Author Contributions: N.S.N.: Conceptualization, Methodology, Validation, Formal Analysis, Investigation, Writing—Original Draft Preparation, Writing—Review and Editing, V.P.P.: Methodology, Investigation, Writing—Original Draft Preparation, Writing—Review and Editing, A.A.P.: Methodology, Investigation, E.Y.G.: Methodology, Investigation, S.V.T.: Methodology, Investigation, Writing—Review and Editing, O.N.M.: Writing—Review and Editing, Supervision, Funding Acquisition. All authors have read and agreed to the published version of the manuscript.

Funding: This research was funded by the Ministry of Science and Higher Education of the Russian Federation within the governmental order for Boreskov Institute of Catalysis (project AAAA-A21-121011390053-4).

Conflicts of Interest: The authors declare no conflict of interest.

References

1. Kwon, Y.; Eichler, J.E.; Mullins, C.B. $NiAl_2O_4$ as a Beneficial Precursor for Ni/Al_2O_3 Catalysts for the Dry Reforming of Methane. *J. CO_2 Util.* **2022**, *63*, 102112. [CrossRef]
2. Alreshaidan, S.B.; Ibrahim, A.A.; Fakeeha, A.H.; Almutlaq, A.M.; Ali, F.A.A.; Al-Fatesh, A.S. Effect of Modified Alumina Support on the Performance of Ni-Based Catalysts for CO_2 Reforming of Methane. *Catalysts* **2022**, *12*, 1066. [CrossRef]
3. Weber, S.; Abel, K.L.; Zimmermann, R.T.; Huang, X.; Bremer, J.; Rihko-Struckmann, L.K.; Batey, D.; Cipiccia, S.; Titus, J.; Poppitz, D.; et al. Porosity and Structure of Hierarchically Porous Ni/Al_2O_3 Catalysts for CO_2 Methanation. *Catalysts* **2020**, *10*, 1471. [CrossRef]
4. Zhou, L.; Li, L.; Wei, N.; Li, J.; Basset, J.-M. Effect of $NiAl_2O_4$ Formation on Ni/Al_2O_3 Stability during Dry Reforming of Methane. *ChemCatChem* **2015**, *7*, 2508–2516. [CrossRef]
5. Gericke, S.M.; Rissler, J.; Bermeo, M.; Wallander, H.; Karlsson, H.; Kollberg, L.; Scardamaglia, M.; Temperton, R.; Zhu, S.; Sigfridsson Clauss, K.G.V.; et al. In Situ H_2 Reduction of Al_2O_3-Supported Ni- and Mo-Based Catalysts. *Catalysts* **2022**, *12*, 755. [CrossRef]
6. Philippov, A.A.; Nesterov, N.N.; Pakharukova, V.P.; Martyanov, O.N. High-Loaded Ni-Based Catalysts Obtained via Supercritical Antisolvent Coprecipitation in Transfer Hydrogenation of Anisole: Influence of the Support. *Appl. Catal. A Gen.* **2022**, *643*, 118792. [CrossRef]
7. Yoon, J.S.; Park, M.B.; Kim, Y.; Hwang, D.W.; Chae, H.-J. Effect of Metal Oxide-Support Interactions on Ethylene Oligomerization over Nickel Oxide/Silica–Alumina Catalysts. *Catalysts* **2019**, *9*, 933. [CrossRef]

8. Chen, Y.; Ren, J. Conversion of Methane and Carbon Dioxide into Synthesis Gas over Alumina-Supported Nickel Catalysts. Effect of Ni-Al_2O_3 Interactions. *Catal. Lett.* **1994**, *29*, 39–48. [CrossRef]
9. Margossian, T.; Larmier, K.; Kim, S.M.; Krumeich, F.; Fedorov, A.; Chen, P.; Müller, C.R.; Copéret, C. Molecularly Tailored Nickel Precursor and Support Yield a Stable Methane Dry Reforming Catalyst with Superior Metal Utilization. *J. Am. Chem. Soc.* **2017**, *139*, 6919–6927. [CrossRef] [PubMed]
10. Shi, Y.; Wang, S.; Li, Y.; Yang, F.; Yu, H.; Chu, Y.; Li, T.; Yin, H. Improving Anti-Coking Properties of Ni/Al_2O_3 Catalysts via Synergistic Effect of Metallic Nickel and Nickel Phosphides in Dry Methane Reforming. *Materials* **2022**, *15*, 3044. [CrossRef]
11. Bian, Z.; Zhong, W.; Yu, Y.; Wang, Z.; Jiang, B.; Kawi, S. Dry Reforming of Methane on Ni/Mesoporous-Al_2O_3 Catalysts: Effect of Calcination Temperature. *Int. J. Hydrogen Energy* **2021**, *46*, 31041–31053. [CrossRef]
12. Zhang, T.; Ai, H.; Liu, Q. La_2O_3-Promoted Ni/Al_2O_3 Catalyst for CO Methanation: Enhanced Catalytic Activity and Stability. *Energy Technol.* **2019**, *7*, 1900531. [CrossRef]
13. Sahli, N.; Petit, C.; Roger, A.C.; Kiennemann, A.; Libs, S.; Bettahar, M.M. Ni Catalysts from $NiAl_2O_4$ Spinel for CO_2 Reforming of Methane. *Catal. Today* **2006**, *113*, 187–193. [CrossRef]
14. Alekseev, E.S.; Alentiev, A.Y.; Belova, A.S.; Bogdan, V.I.; Bogdan, T.V.; Bystrova, A.V.; Gafarova, E.R.; Golubeva, E.N.; Grebenik, E.A.; Gromov, O.I.; et al. Supercritical Fluids in Chemistry. *Russ. Chem. Rev.* **2020**, *89*, 1337–1427. [CrossRef]
15. Nesterov, N.S.; Simentsova, I.I.; Yudanov, V.F.; Martyanov, O.N. A Comparative FMR Study of the Reduction of Co-Containing Catalysts for the Fischer-Tropsch Process in Hydrogen and Supercritical Isopropanol. *J. Struct. Chem.* **2016**, *57*, 90–96. [CrossRef]
16. Anastas, P.T.; Warner, J.C. *Green Chemistry: Theory and Practice*; Oxford University Press: Oxford, UK, 2000; ISBN 978-0-19-850698-0.
17. Siril, P.F.; Türk, M. Synthesis of Metal Nanostructures Using Supercritical Carbon Dioxide: A Green and Upscalable Process. *Small* **2020**, *16*, 2001972. [CrossRef]
18. Hutchings, G.J. Catalyst Synthesis Using Supercritical Carbon Dioxide: A Green Route to High Activity Materials. *Top. Catal.* **2009**, *52*, 982–987. [CrossRef]
19. Martín, A.; Cocero, M.J. Numerical Modeling of Jet Hydrodynamics, Mass Transfer, and Crystallization Kinetics in the Supercritical Antisolvent (SAS) Process. *J. Supercrit. Fluids* **2004**, *32*, 203–219. [CrossRef]
20. Kondrat, S.A.; Smith, P.J.; Wells, P.P.; Chater, P.A.; Carter, J.H.; Morgan, D.J.; Fiordaliso, E.M.; Wagner, J.B.; Davies, T.E.; Lu, L.; et al. Stable Amorphous Georgeite as a Precursor to a High-Activity Catalyst. *Nature* **2016**, *531*, 83–87. [CrossRef]
21. Smith, P.J.; Kondrat, S.A.; Carter, J.H.; Chater, P.A.; Bartley, J.K.; Taylor, S.H.; Spencer, M.S.; Hutchings, G.J. Supercritical Antisolvent Precipitation of Amorphous Copper-Zinc Georgeite and Acetate Precursors for the Preparation of Ambient-Pressure Water-Gas-Shift Copper/Zinc Oxide Catalysts. *ChemCatChem* **2017**, *9*, 1621–1631. [CrossRef]
22. Franco, P.; Sacco, O.; De Marco, I.; Vaiano, V. Zinc Oxide Nanoparticles Obtained by Supercritical Antisolvent Precipitation for the Photocatalytic Degradation of Crystal Violet Dye. *Catalysts* **2019**, *9*, 346. [CrossRef]
23. Da Silva, E.P.; Winkler, M.E.G.; Giufrida, W.M.; Cardozo-Filho, L.; Alonso, C.G.; Lopes, J.B.O.; Rubira, A.F.; Silva, R. Effect of Phase Composition on the Photocatalytic Activity of Titanium Dioxide Obtained from Supercritical Antisolvent. *J. Colloid Interface Sci.* **2019**, *535*, 245–254. [CrossRef] [PubMed]
24. Marin, R.P.; Ishikawa, S.; Bahruji, H.; Shaw, G.; Kondrat, S.A.; Miedziak, P.J.; Morgan, D.J.; Taylor, S.H.; Bartley, J.K.; Edwards, J.K.; et al. Supercritical Antisolvent Precipitation of TiO_2 with Tailored Anatase/Rutile Composition for Applications in Redox Catalysis and Photocatalysis. *Appl. Catal. A Gen.* **2015**, *504*, 62–73. [CrossRef]
25. Nesterov, N.S.; Shalygin, A.S.; Pakharukova, V.P.; Glazneva, T.S.; Martyanov, O.N. Mesoporous Aerogel-like Al-Si Oxides Obtained via Supercritical Antisolvent Precipitation of Alumina and Silica Sols. *J. Supercrit. Fluids* **2019**, *149*, 110–119. [CrossRef]
26. Nesterov, N.S.; Pakharukova, V.P.; Martyanov, O.N. Water as a Cosolvent—Effective Tool to Avoid Phase Separation in Bimetallic Ni-Cu Catalysts Obtained via Supercritical Antisolvent Approach. *J. Supercrit. Fluids* **2017**, *130*, 133–139. [CrossRef]
27. Nesterov, N.S.; Paharukova, V.P.; Yakovlev, V.A.; Martyanov, O.N. The Facile Synthesis of Ni–Cu Catalysts Stabilized in SiO_2 Framework via a Supercritical Antisolvent Approach. *J. Supercrit. Fluids* **2016**, *112*, 119–127. [CrossRef]
28. Nesterov, N.S.; Shalygin, A.S.; Pakharukova, V.P.; Martyanov, O.N. Coprecipitation of Au Clusters and Alumina Sol in Supercritical CO_2—The Facile Way to Stabilize Gold Nanoparticles within Oxide Matrix. *J. Sol. Gel. Sci. Technol.* **2019**, *92*, 523–528. [CrossRef]
29. Nesterov, N.S.; Shalygin, A.S.; Glazneva, T.S.; Pakharukova, V.P.; Martyanov, O.N. The Facile Synthesis of Aerogel-like Alumina Highly-Loaded with Gold Nanoparticles. *Gold Bull.* **2021**, *54*, 69–74. [CrossRef]
30. Nesterov, N.S.; Smirnov, A.A.; Pakharukova, V.P.; Yakovlev, V.A.; Martyanov, O.N. Advanced Green Approaches for the Synthesis of NiCu-Containing Catalysts for the Hydrodeoxygenation of Anisole. *Catal. Today* **2021**, *379*, 262–271. [CrossRef]
31. Philippov, A.; Nesterov, N.; Pakharukova, V.; Kozhevnikov, I.; Martyanov, O. Advanced High-Loaded Ni–Cu Catalysts in Transfer Hydrogenation of Anisole: Unexpected Effect of Cu Addition. *Catalysts* **2022**, *12*, 1307. [CrossRef]
32. Yang, Y.; Liu, X.; Xu, Y.; Gao, X.; Dai, Y.; Tang, Y. Palladium-Incorporated α-MoC Mesoporous Composites for Enhanced Direct Hydrodeoxygenation of Anisole. *Catalysts* **2021**, *11*, 370. [CrossRef]
33. Mudhulu, S.; Gong, Z.-J.; Ku, H.-C.; Lu, Y.-H.; Yu, W.-Y. Recent Advances in Heterogeneous Catalytic Hydrodeoxygenation of Biomass-Derived Oxygenated Furanics Mediated by Formic Acid. *Mater. Today Sustain.* **2022**, *19*, 100199. [CrossRef]
34. Song, L.; Ouyang, Y.; Huang, S.; Li, Z.; Sun, M. Insight into Liquefaction Process of Sawdust with Hydrogen Donor Solvents. *Biomass Bioenergy* **2022**, *160*, 106444. [CrossRef]
35. Xu, H.; Li, H. Alcohol-Assisted Hydrodeoxygenation as a Sustainable and Cost-Effective Pathway for Biomass Derivatives Upgrading. *J. Energy Chem.* **2022**, *73*, 133–159. [CrossRef]

36. Philippov, A.A.; Chibiryaev, A.M.; Martyanov, O.N. Raney®Nickel-Catalyzed Hydrodeoxygenation and Dearomatization under Transfer Hydrogenation Conditions—Reaction Pathways of Non-Phenolic Compounds. *Catal. Today* **2020**, *355*, 35–42. [CrossRef]
37. Philippov, A.A.; Chibiryaev, A.M.; Martyanov, O.N. Catalyzed Transfer Hydrogenation by 2-Propanol for Highly Selective PAHs Reduction. *Catal. Today* **2021**, *379*, 15–22. [CrossRef]
38. Shafaghat, H.; Tsang, Y.F.; Jeon, J.K.; Kim, J.M.; Kim, Y.; Kim, S.; Park, Y.K. In-Situ Hydrogenation of Bio-Oil/Bio-Oil Phenolic Compounds with Secondary Alcohols over a Synthesized Mesoporous Ni/CeO_2 Catalyst. *Chem. Eng. J.* **2020**, *382*, 122912. [CrossRef]
39. Chen, H.; Xu, Q.; Zhang, D.; Liu, W.; Liu, X.; Yin, D. Highly Efficient Synthesis of γ-Valerolactone by Catalytic Conversion of Biomass-Derived Levulinate Esters over Support-Free Mesoporous Ni. *Renew. Energy* **2021**, *163*, 1023–1032. [CrossRef]
40. Gilkey, M.J.; Xu, B. Heterogeneous Catalytic Transfer Hydrogenation as an Effective Pathway in Biomass Upgrading. *ACS Catal.* **2016**, *6*, 1420–1436. [CrossRef]
41. Philippov, A.A.A.; Chibiryaev, A.M.; Martyanov, O.N. Base-Free Transfer Hydrogenation of Menthone by Sub- and Supercritical Alcohols. *J. Supercrit. Fluids* **2019**, *145*, 162–168. [CrossRef]
42. Jin, W.; Pastor-Pérez, L.; Villora-Picó, J.J.; Sepúlveda-Escribano, A.; Gu, S.; Reina, T.R. Investigating New Routes for Biomass Upgrading: "H_2-Free" Hydrodeoxygenation Using Ni-Based Catalysts. *ACS Sustain. Chem. Eng.* **2019**, *7*, 16041–16049. [CrossRef]
43. Zangouei, M.; Moghaddam, A.Z.; Arasteh, M. The Influence of Nickel Loading on Reducibility of NiO/Al_2O_3 Catalysts Synthesized by Sol-Gel Method. *Chem. Eng. Res. Bull.* **2010**, *14*, 97–102. [CrossRef]
44. Gamliel, D.P.; Karakalos, S.; Valla, J.A. Liquid Phase Hydrodeoxygenation of Anisole, 4-Ethylphenol and Benzofuran Using Ni, Ru and Pd Supported on USY Zeolite. *Appl. Catal. A Gen.* **2018**, *559*, 20–29. [CrossRef]
45. Khan, T.S.; Singh, D.; Samal, P.P.; Krishnamurty, S.; Dhepe, P.L. Mechanistic Investigations on the Catalytic Transfer Hydrogenation of Lignin-Derived Monomers over Ru Catalysts: Theoretical and Kinetic Studies. *ACS Sustain. Chem. Eng.* **2021**, *9*, 14040–14050. [CrossRef]
46. Rios-Escobedo, R.; Ortiz-Santos, E.; Colín-Luna, J.A.; Díaz de León, J.N.; del Angel, P.; Escobar, J.; de los Reyes, J.A. Anisole Hydrodeoxygenation: A Comparative Study of Ni/TiO_2-ZrO_2 and Commercial TiO_2 Supported Ni and NiRu Catalysts. *Top. Catal.* **2022**, *65*, 1448–1461. [CrossRef]
47. Li, S.; Guo, L.; He, X.; Qiao, C.; Tian, Y. Synthesis of Uniform Ni Nanoparticles Encapsulated in ZSM–5 for Selective Hydrodeoxygenation of Phenolics. *Renew. Energy* **2022**, *194*, 89–99. [CrossRef]
48. Zhang, Y.; Fan, G.; Lin, Y.; Yang, L.; Li, F. Synergies of Surface-Interface Multiple Active Sites over Al-Zr Oxide Solid Solution Supported Nickel Catalysts for Enhancing the Hydrodeoxygenation of Anisole. *Appl. Catal. A Gen.* **2022**, *631*, 118481. [CrossRef]
49. Vargas-Villagrán, H.; Flores-Villeda, M.A.; Puente-Lee, I.; Solís-Casados, D.A.; Gómez-Cortés, A.; Díaz-Guerrero, G.; Klimova, T.E. Supported Nickel Catalysts for Anisole Hydrodeoxygenation: Increase in the Selectivity to Cyclohexane. *Catal. Today* **2018**, *349*, 26–41. [CrossRef]
50. Taghvaei, H.; Moaddeli, A.; Khalafi-Nezhad, A.; Iulianelli, A. Catalytic Hydrodeoxygenation of Lignin Pyrolytic-Oil over Ni Catalysts Supported on Spherical Al-MCM-41 Nanoparticles: Effect of Si/Al Ratio and Ni Loading. *Fuel* **2021**, *293*, 120493. [CrossRef]
51. Egami, T.; Billinge, S.J.L. *Underneath the Bragg Peaks Structural Analysis of Complex Materials*; Elsevier: Pergamon, Turkey, 2012.
52. Qiu, X.; Thompson, J.W.; Billinge, S.J.L. PDFgetX2: A GUI-Driven Program to Obtain the Pair Distribution Function from X-Ray Powder Diffraction Data. *J. Appl. Crystallogr.* **2004**, *37*, 678. [CrossRef]
53. Farrow, C.L.; Juhas, P.; Liu, J.W.; Bryndin, D.; Božin, E.S.; Bloch, J.; Proffen, T.; Billinge, S.J.L. PDFfit2 and PDFgui: Computer Programs for Studying Nanostructure in Crystals. *J. Phys. Condens. Matter* **2007**, *19*, 335219. [CrossRef] [PubMed]